

Segmentation by Classification for Through-the-Wall Radar Imaging Using Polarization Signatures

Ahmed A. Mostafa, *Student Member, IEEE*, Christian Debes, *Member, IEEE*, and Abdelhak M. Zoubir, *Fellow, IEEE*

Abstract—A scheme for target detection using segmentation by classification is proposed. The scheme is applied to through-the-wall microwave images obtained using frequency-domain back-projection in a wideband radar. We consider stationary targets where Doppler and change-detection-based techniques are inapplicable. The proposed scheme uses features from polarimetric images to segment and classify the image observations into target, clutter, and noise segments. We map target polarization signatures from copolarized and cross-polarized target returns to a pixel-by-pixel feature space, then oversegment the image to homogeneous regions called superpixels depending on this feature space. The features of each superpixel are used subsequently to group homogeneous superpixels into clusters. The clusters are then classified using decision trees. Real data collected using an indoor radar imaging scanner are used for performance validation.

Index Terms—Classification, decision trees, polarimetric, radar imaging, segmentation, superpixels, through-the-wall.

I. INTRODUCTION

THROUGH-the-wall radar imaging (TWRI) is an evolving technology that gained much attention in the last decade [1]–[4]. It allows to sense through visually opaque building material and man-made structures using electromagnetic wave propagation which has numerous applications in civil engineering, search and rescue operations, cultural heritage diagnostics, law enforcement, and military applications [1], [2], [5], [6]. TWRI is faced with many challenges, including detection and classification of a large variety of possible indoor targets in the presence of multipath and unwanted wall signal attenuation and dispersive effects [6]–[9]. In addition, when considering stationary targets, Doppler signatures and change detection techniques become ineffective, and one has to perform detection and classification in the image domain, as a postprocessing step to beamforming.

The radar images of stationary targets obtained through a wall are subject to strong artifacts, which could visually appear as targets in intensity and spatial concentration. Human interac-

tive systems do not work in such environments. To avoid false alarms, robust computer-based systems are sought for.

Modeling and imaging of fixed targets behind walls and inside enclosed structures have been an active area of research [10]–[14]. Research on TWRI target detection has been developed in two domains, the data domain and the image domain. Data-domain target detection involves waveform design to improve target detection using matched illumination with partial or full prior knowledge of the target radar cross section (RCS) over angle and frequency [15]–[18], which works well under specific assumptions about the targets and propagation environments. With multiple targets and unknown target orientation, it becomes less effective. Image-domain-based target detection [5], [19]–[22] handles multiple targets with no prior assumptions on the target RCS, but it faces the challenge of operating with limited bandwidth and insufficient physical or synthesized array aperture, thus disallowing high-resolution-based target analysis and classification. Detection in the image domain has been proposed using centralized [5] as well as decentralized [23] approaches. The common aim within both approaches is to deduce a single binary 3-D reference image from a set of 3-D TWRI images, to decide the presence or absence of targets. However, all these approaches make use of single polarization data, while multipolarization data can capture different aspects of a target and are thus promising to improve the overall detection result [24], [25].

Existing work in polarimetric imaging for TWRI applications includes [26]–[29]. In [26], polarization signatures were used to detect a rifle in TWRI images using the cross- to copolarization return ratio. In [27], the authors consider polarization difference imaging that shows improved enhancement in terms of image quality. In [28], a multiplicative combination technique of co- and cross-polarized time-difference images is considered to reduce the effect of ghost targets that appear in TWRI images due to multipath propagation. As such, the image quality is strongly improved which facilitates target detection. In [29], the authors utilize multipolarization images for TWRI to improve the performance of the adaptive target detection techniques proposed in [5], [19], and [30]. The technique improves detection by utilizing polarization diversity and accounting for changing image intensity distributions as a function of transmitter-receiver co- and cross-polarizations.

The contribution in this paper is a framework for target detection using segmentation by classification, including exploitation of target polarization signatures. Each B-Scan of the 3-D TWRI image is oversegmented to homogeneous regions without restriction on the shape of the region or the number of regions. These regions are then clustered together using

Manuscript received July 15, 2011; revised November 17, 2011; accepted December 18, 2011. Date of publication March 1, 2012; date of current version August 22, 2012. This work is supported by the ‘Excellence Initiative’ of the German Federal and State Governments and the Graduate School of Computational Engineering at Technische Universität Darmstadt.

A. A. Mostafa and A. M. Zoubir are with the Signal Processing Group, Institute of Telecommunications, Technische Universität Darmstadt, 64283 Darmstadt, Germany (e-mail: amostafa@spg.tu-darmstadt.de; zoubir@spg.tu-darmstadt.de).

C. Debes is with AGT Group (R&D) GmbH, 64295 Darmstadt, Germany (e-mail: cdebes@agtgermany.com).

Color versions of one or more of the figures in this paper are available online at <http://ieeexplore.ieee.org>.

Digital Object Identifier 10.1109/TGRS.2011.2181951

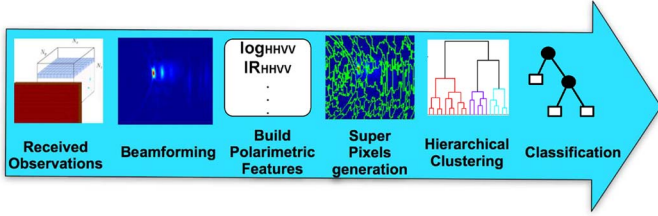


Fig. 1. General steps of segmentation by classification.

agglomerative clustering to form three clusters. The resulting clustered or superpixels data set is divided into a training set and a testing set. The training set is used to build a classifier using a random forests algorithm [31], which is then tested using the testing data set. A diagram summarizing the general steps of the proposed algorithm is shown in Fig. 1.

In Section II, the wideband delay-and-sum beamforming (DSBF) used to generate radar images through walls is reviewed. Section III discusses the use of polarization signatures in TWRI in the image domain. Section IV details the use of polarization signatures to oversegment B-Scan images into homogeneous regions. Section V presents the use of clustering to group similar segments in clusters, whereas Section VI discusses the use of decision trees for classification of these clusters into target, clutter, and noise clusters. Section VII presents experimental results, and we draw conclusions in Section VIII. All real data examples included in this paper are obtained from TWRI measurements collected at the Radar Imaging Lab at Villanova University, Villanova, PA, USA.

II. IMAGE FORMATION

In this section, the DSBF [11], [13] used to generate radar images through walls is reviewed. We note that, for TWRI applications and data examples treated in this paper, we assume perfect knowledge or correctly estimated values of the wall parameters. Estimation techniques of the wall thickness and dielectric constant can be found in [3], [4] and references therein.

A. Wideband Delay and Sum Beamformer

We hereby follow the same scheme as in [11]. In the sequel, we consider a uniform 1-D array of N transceivers using a wideband pulse. A wideband pulse is approximated using a stepped frequency approach. The advantages of the stepped-frequency-based imaging are multifold [11]. Stepped frequency implies the use of M monochromatic signals with regularly spaced frequencies that cover the desired bandwidth. Assuming that the scene of interest can be described by P discrete targets with reflectivities σ_p , $p = 0, \dots, P-1$, the received signal, which is a function of sensor element n , $n = 0, \dots, N-1$ and frequency m , $m = 0, \dots, M-1$, can be written as

$$y[m, n] = \sum_{p=0}^{P-1} \sigma_p w_m e^{-j2\pi f_m \tau_{pn}} \quad (1)$$

where f_m denotes the m th step frequency, τ_{pn} is the round trip delay between the p th target and the n th receiver and w_m are weighting factors. A derivation can be found in [11]. Assuming the region of interest to be identified by $Q = N_x \cdot N_y$ grid

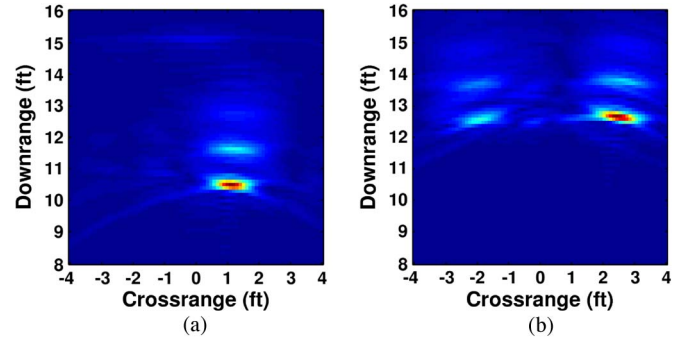


Fig. 2. Sample beamformed images using DSBF beamforming. (a) One target. (b) Two targets.

points, where N_x is the number of points in crossrange and N_y is the number of points in downrange, one can steer the beam at every pixel q with $q = 0, \dots, Q-1$ and the complex valued image (B-Scan) can be obtained by [11]

$$I(q) = \frac{1}{MN} \sum_{n=0}^{N-1} \sum_{m=0}^{M-1} y[m, n] e^{j2\pi f_m \tau_{qn}} \quad (2)$$

where τ_{qn} is the delay compensation for the n th receiver, steering the beam at position q . The resulting B-Scan images (2-D cuts through the 3-D volume) at the height of the target center are shown in Fig. 2.

III. POLARIZATION SIGNATURES SETS

Polarimetric SAR images carry more information about the imaged scene than the usual single polarized channel images [32]–[34]. Many attempts to find or use optimal combination of the information available from the different polarimetric channels have been made, including [35]–[41].

Let \mathbf{X}_s denote the polarimetric vector of the complex measurements at pixel site s . The full polarimetric vector of the complex measurements for a reciprocal medium has three unique elements and is usually defined as [40]

$$\mathbf{X}_s = [S_{HH} \ S_{HV} \ S_{VV}]^T \quad (3)$$

where S_{HV} is the complex amplitude of the H - (horizontal) polarized return given that the transmitted signal is V - (vertically) polarized. For a homogeneous region, the fully polarimetric target properties for uniform distributed scatterers can be described by the polarimetric covariance matrix [41]

$$\mathbf{C}_1 = \langle \mathbf{X}_s^{*T} \mathbf{X}_s \rangle = \begin{pmatrix} E(S_{HH} S_{HH}^*) & E(S_{HH} S_{HV}^*) & E(S_{HH} S_{VV}^*) \\ E(S_{HV} S_{HH}^*) & E(S_{HV} S_{HV}^*) & E(S_{HV} S_{VV}^*) \\ E(S_{VV} S_{HH}^*) & E(S_{VV} S_{HV}^*) & E(S_{VV} S_{VV}^*) \end{pmatrix} \quad (4)$$

where $E(\cdot)$ is the expected value and $*$ defines the complex conjugate operation. Hence, a possible mode of unsupervised selection of the classes of polarimetric backscatter is to perform clustering on a feature vector that comprises the parameters, composing the matrix \mathbf{C}_1 [42] or derived from them. For practical implementation, the expected value $E(\cdot)$ is replaced by the sample mean. In this section, we will discuss some of

the polarization signatures or features used in the literature and considered in our algorithms.

- (a) Thresholded intensity features: The absolute value of each complex component is thresholded using the automatic level thresholding algorithm [43] so that we have three features in the thresholded intensity feature vector

$$\mathbf{T} = [T_{HH} \ T_{HV} \ T_{VV}]^T. \quad (5)$$

- (b) Normalized phase difference: It is the phase difference between any two complex polarized components [33]

$$\Psi = \arg(S_i S_j^*). \quad (6)$$

Usually, the components considered are the two copolarized components HH and VV.

- (c) Normalized intensity ratio: It is the intensity ratio between any two complex polarized components [33]. We define the vector

$$\mathbf{IR} = \begin{bmatrix} |S_{HH}|^2 & |S_{HH}|^2 & |S_{HV}|^2 \\ |S_{VV}|^2 & |S_{HV}|^2 & |S_{VV}|^2 \end{bmatrix}^T. \quad (7)$$

We will refer to these features as IR_{HHVV} , IR_{HHHV} , and IR_{VVHV} , respectively.

- (d) Odd and even bounce: In [44], the authors used different features to discriminate targets from clutter in SAR images. One of the features the authors used are the odd and even energy return features

$$E_{odd} = \frac{|S_{HH} + S_{VV}|^2}{2} \quad (8)$$

$$E_{even} = \frac{|S_{HH} - S_{VV}|^2}{2} + 2|S_{HV}|^2. \quad (9)$$

The odd-bounce channel corresponds to the radar return from a flat plate or a trihedral; the even-bounce channel corresponds to the radar return from a dihedral. The usefulness of these polarimetric features resides in the fact that a few dihedral structures exist in natural clutter, but these structures are sufficient to describe most man-made targets. Natural clutter tends to exhibit more odd bounce reflected energy than even-bounce reflected energy [44].

- (e) Real part and imaginary part of normalized product: in [41], many representations for the covariance matrix that characterize fully polarimetric data are introduced. These include features that mainly consist of intensities, phase differences, normalized or averaged products, and the real and imaginary parts of the averaged product of different polarizations

$$\mathbf{AP}_{\text{RI}} = \begin{pmatrix} \text{Re}[\langle S_{HH} S_{VV}^* \rangle] \\ \text{Im}[\langle S_{HH} S_{VV}^* \rangle] \\ \text{Re}[\langle S_{HH} S_{HV}^* \rangle] \\ \text{Im}[\langle S_{HH} S_{HV}^* \rangle] \\ \text{Re}[\langle S_{HV} S_{VV}^* \rangle] \\ \text{Im}[\langle S_{HV} S_{VV}^* \rangle] \end{pmatrix} \quad (10)$$

where the $\langle \cdot \rangle$ denotes the average over a local set of target samples. We will refer to these features as Re_{HHVV^*} , Im_{HHVV^*} , Re_{HHHV^*} , Im_{HHHV^*} , Re_{HVVV^*} and Im_{HVVV^*} , respectively.

- (f) Logarithmic features: in [42], the logarithm of the intensities, product magnitude, and phase difference of different polarizations is suggested as characterizing features

$$\mathbf{IP}_{\text{log}} = \begin{pmatrix} 10 \log_{10} (\langle |S_{HH}|^2 \rangle) \\ 10 \log_{10} (\langle |S_{VV}|^2 \rangle) \\ 10 \log_{10} (\langle |S_{HV}|^2 \rangle) \\ 10 \log_{10} (|\langle S_{HH} S_{VV}^* \rangle|) \\ 10 \frac{\arg(S_{HH} S_{VV}^*)}{\log(10)} \end{pmatrix}. \quad (11)$$

The first three coefficients represent the backscatter cross sections of the surface element in dB at three different linear polarizations. The fourth component measures the magnitude of the HH-VV correlation function, and the fifth one is proportional to the HH-VV phase difference. We will refer to these features as \log_{HH} , \log_{HV} , \log_{VV} , \log_{HHVV^*} , and \log_{PHHV^*} , respectively. The advantages of operating in the log domain instead of the linear domain are twofold. First, in the log domain, image speckle has the statistical characteristics of additive noise with a power level not varying much across the image, therefore rendering clustering robust to the presence of image speckle. Second, the cross-polarized terms (i.e., HV) are often several orders of magnitude smaller than the copolarized terms (i.e., HH or VV), which requires arbitrary weighting of the different channels. In the log domain, the difference between the copolarized and the cross-polarized terms is measured in dB and hence, is independent of the difference in absolute magnitude between each channel. Weighting of the different channels is thus not necessary [42].

The proposed feature vector at each pixel q will contain the thresholded intensity features, logarithmic features, intensity ratio, real and imaginary parts of the averaged products, and the odd and even bounce returns as follows:

$$\mathbf{F}_q = [\mathbf{T} \ \mathbf{IP}_{\text{log}} \ \mathbf{IR} \ \mathbf{AP}_{\text{RI}} \ E_{odd} \ E_{even}]^T \quad (12)$$

which contains 19 features in total. Table I lists the features in brief.

IV. SEGMENTATION AND SUPERPIXELS

All existing image-domain target detection algorithms in TWRI use pixel-grid as the underlying representation, cf. [5], [19]–[22]. However, the pixel-grid is not a natural representation of visual scenes. It is rather an “artifact” of a digital imaging process. It would be more natural, and more efficient, to work with perceptually meaningful entities, obtained from a low-level grouping process [45], [46]. For that, we apply over-segmentation to segment the image into regions with homogeneous characteristics.

In this section, we present a preprocessing stage to group pixels into homogeneous regions called “superpixels.” To create the superpixels for our TWRI B-Scans, we used the quick shift algorithm [47] for segmentation. Unlike other superpixelization schemes, such as the ones based on normalized cuts [45], quick shift produces superpixels that are not fixed in approximate size or number. A complex image with many fine scale image

TABLE I
FEATURES, THEIR CORRESPONDING NUMBER, AND THE ABBREVIATIONS TO BE USED IN THE REMAINDER OF THE PAPER

No.	Feature
1-3	Thresholded intensities T_{HH} , T_{HV} and T_{VV}
4-6	Logarithmic intensities \log_{HH} , \log_{HV} and \log_{VV}
7	Logarithmic absolute of the product $HH VV^* \rightarrow \log_{HHVV^*}$
8	Logarithmic phase of the product $HH VV^* \rightarrow \log_{PHHV^*}$
9-11	Intensity ratios IR_{HHVV} , IR_{HHHV} and IR_{VVHV}
12, 14, 16	Real part of the normalized products Re_{HHVV^*} , Re_{HHHV^*} and Re_{HVVV^*}
13, 15, 17	Imaginary part of the normalized products Im_{HHVV^*} , Im_{HHHV^*} and Im_{HVVV^*}
18-19	Odd and even bounce energies E_{odd} and E_{even}

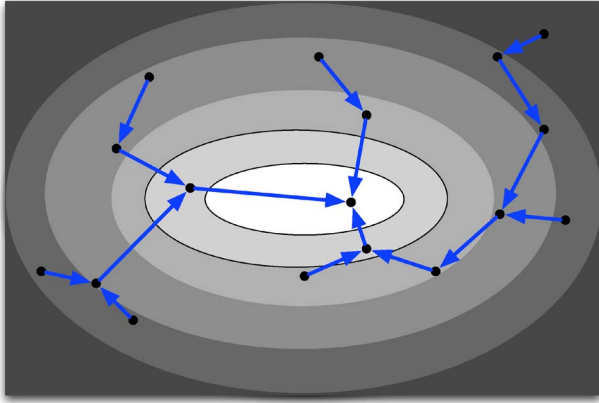


Fig. 3. Tree forming illustration using quick shift. The black dots represent (some of) the data points, and the intensity of the image is proportional to the Parzen density estimate $E(q)$ from (13). Redrawn from [47].

structures may have many more superpixels than a simple one, and there is no parameter which puts a penalty on the boundary, leading to superpixels which are quite varied in size and shape [48].

From (2) of Section II, we can get the complex B-Scan image I for each height. Combining the different B-Scans for all heights will give a 3-D image for the whole scene. Each pixel has an associated vector of features as described in Section III, then the feature vector associated with each pixel as in (12) can be identified as $\mathbf{F}_q(d)$ where $d = 0, \dots, D-1$ and D is the number of features.

Quick shift is a mode seeking algorithm which links each pixel to its nearest neighbor which has an increase in the estimate of the density. These links form a tree where the root of the tree is the pixel, which corresponds to the highest mode in the image [47]. Fig. 3 shows a simple illustration of how quick shift forms the tree. Quick shift regards each pixel q , $q = 0, \dots, Q-1$, as a sample from a $D+2$ dimensional vector space. It then calculates the Parzen density estimate (with a Gaussian kernel of standard deviation σ) [49]

$$\begin{aligned}
 E(q) &= P(x_q, y_q, \mathbf{F}_q) \\
 &= \sum_{j=0}^{J-1} \frac{1}{(2\pi\sigma)^{D+2}} \\
 &\quad \times \exp \left(-\frac{1}{2\sigma^2} \begin{bmatrix} x_q - x_j \\ y_q - y_j \\ \mathbf{F}_q - \mathbf{F}_j \end{bmatrix}^T \begin{bmatrix} x_q - x_j \\ y_q - y_j \\ \mathbf{F}_q - \mathbf{F}_j \end{bmatrix} \right) \quad (13)
 \end{aligned}$$

where $j = 0, 1, \dots, J-1$ denotes the neighboring pixel j , J is the number of neighboring pixels, x and y are the physical

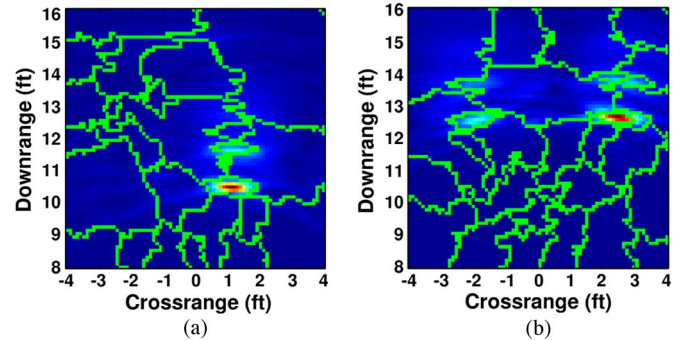


Fig. 4. Typical results for quick shift segmentation of the images from Fig. 2. (a) One target. (b) Two targets.

coordinates of the pixel. Then, quick shift constructs a tree of pixels, connecting each image pixel to its nearest neighbor which has a greater density value. Formally, $E(j) > E(q)$ if, and only if [49]

$$P(x_j, y_j, \mathbf{F}_j) > P(x_q, y_q, \mathbf{F}_q). \quad (14)$$

Each pixel (x_q, y_q) is connected to the closest higher density pixel $parent(x'_q, y'_q)$ that achieves the minimum distance in

$$\text{dist}(q) = \min_{P(j) > P(q)} \left((x_q - x_j)^2 + (y_q - y_j)^2 + \|\mathbf{F}_q - \mathbf{F}_j\|_2^2 \right). \quad (15)$$

The algorithm connects all the points into a single tree. Modes are then recovered by breaking the branches of the tree that are longer than a threshold τ . We used the quick shift implementation in the library VLFeat [49]. A typical segmentation result using quick shift applied to B-Scans of one and two target scenes using the feature set described on Section III is shown in Fig. 4.

V. CLUSTERING

The aim is to cluster the superpixels resulting from the previous stage to a maximum of three clusters for each B-Scan, corresponding to targets, clutter, and noise. We note that clustering is an optional step and may not be used if the number of superpixels is low. In this case, the superpixels can be used directly for training and testing of the classifier presented in the next section. To achieve this, we first calculate a single feature vector for each superpixel based on the features of all underlying pixels contained in a superpixel. We take the median for each feature throughout all pixels that belong to this superpixel to be the new value of this feature for this superpixel.

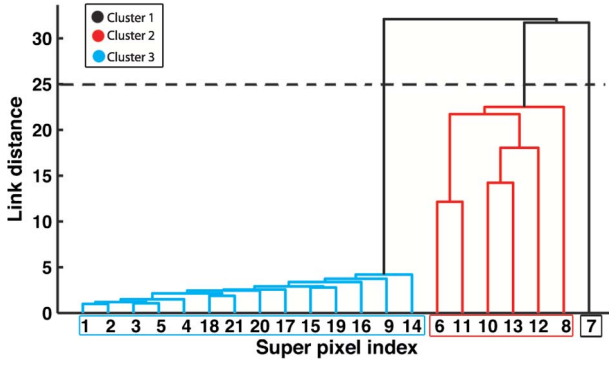


Fig. 5. Typical dendrogram to visualize clustering for a two target B-Scan. Different colors represent different clusters. The horizontal dashed line illustrates where to cut to get three clusters.

If ξ_s is the set of pixels belonging to super pixel s , then the new value for the feature d in the superpixel feature vector \mathbf{FS}_s

$$\mathbf{FS}_s(d) = \tilde{\mathbf{F}}_{q \in \xi_s}(d) \quad (16)$$

where s is the superpixel index, $s = 0, \dots, S-1$, S is the number of superpixels, $q \in \xi_s$ denotes the group of pixels that belong to superpixel s , and $d = 0, 1, \dots, D-1$ is the feature index.

We use hierarchical agglomerative clustering [50], [51] to group the superpixels into clusters, using the Euclidean distance to calculate the distances between the superpixels, i.e., the distance between two feature vectors \mathbf{FS}_1 and \mathbf{FS}_2 is given by

$$\|\mathbf{FS}_1 - \mathbf{FS}_2\|_2 = \sqrt{\sum_d (\mathbf{FS}_1(d) - \mathbf{FS}_2(d))^2}. \quad (17)$$

Subsequently, a linkage function is used to group the superpixels hierarchically into clusters, a single linkage [50], [51] (also known as nearest neighbor or shortest distance) method is used to calculate the distance matrix between elements according to the minimum distance. The result of linkage can be represented visually as a dendrogram, the numbers along the horizontal axis represent the indices of the superpixels. The links between superpixels are represented as upside-down U-shaped lines. The height of U indicates the distance between the superpixels. A typical dendrogram result from clustering the two target image from Fig. 4 is shown in Fig. 5.

VI. CLASSIFICATION WITH RANDOM FORESTS

In this section, we propose a sequential classification scheme using random forests ensemble trees classifier [31]. Previous work regarding stationary target classification for TWRI includes [52], [53] where a minimum Mahalanobis distance classifier is used to classify targets using 3-D statistical models. Further, in [20], iterative conditional modes (ICM) segmentation was considered to divide the TWRI image into target and noise, then nearest-neighbor classifier and support vector machines were used for further classification using superquadrics features.

Decision trees are one of the most popular classification algorithms used in data mining and machine learning to create knowledge structures that guide the decision-making process [54]–[56]. Thus, they have the ability to handle high-dimensional data well and to ignore irrelevant features [57]. These are desirable properties for the problem at hand.

In our classification problem, we are given data on a set of N superpixels for training, $\chi = (\mathbf{FS}_1, O_1), \dots, (\mathbf{FS}_N, O_N)$, where \mathbf{FS}_n is a vector of descriptors and O_n is the corresponding n class label. Our goal is to find a model for predicting the values of O from new \mathbf{FS} values. Classification tree methods yield rectangular sets A_j such that the predicted value of O is j if \mathbf{FS} belongs to A_j for $j = 1, 2, \dots, J$ where J is the number of disjoint sets. By recursively partitioning the data set one \mathbf{FS} variable at a time, the splits resulting from using each of the predictors are examined. The best split that maximizes homogeneity for both its parts is chosen. Then, this procedure is repeated until there are no more possible splits or a stopping criterion is met. Deciding which is the “best” split is still an active research area, the most used method is the classification and regression trees [54] which measures the impurities at each split using the Gini [58] impurity algorithm. Let t_p be a parent node, t_l, t_r the left and right child nodes, respectively, χ a data set with D descriptors, N the number of observations, and K the number of classes. At each split, we have \mathbf{FS}_d^R which is the best threshold for the descriptor \mathbf{FS}_d that gives maximum homogeneity for each part. At the parent node t_p , the impurity is constant for all possible splits, so the change of impurity for the left and right nodes is calculated as follows [59]:

$$\Delta i(t) = i(t_p) - P_l(t_l) - P_r(t_r) \quad (18)$$

where P_l and P_r are the probabilities of the left and the right nodes. The objective is to solve for

$$\arg \max_{\mathbf{FS}_d \leq \mathbf{FS}_d^R} \Delta [i(t)] = \arg \max_{\mathbf{FS}_d \leq \mathbf{FS}_d^R} [i(t_p) - P_l(t_l) - P_r(t_r)]. \quad (19)$$

This means that all possible values of the descriptors will be searched for the best split $\mathbf{FS}_d \leq \mathbf{FS}_d^R$ that will maximize the change of impurity $\Delta i(t)$. As mentioned before, the Gini function will be used as impurity function here, which states that

$$I(t) = 1 - \sum_{k=1}^K p^2(k|t) \quad (20)$$

where $k = 1, 2, \dots, K$ is the class index and $p(k|t)$ is the probability of class k given node t . Substituting (20) in (19) gives

$$\arg \max_{\mathbf{FS}_d \leq \mathbf{FS}_d^R} \Delta [i(t)] = \arg \max_{\mathbf{FS}_d \leq \mathbf{FS}_d^R} \left[- \sum_{k=1}^K p^2(k|t_p) + P_l \sum_{k=1}^K p^2(k|t_l) + P_r \sum_{k=1}^K p^2(k|t_r) \right] \quad (21)$$

which is the problem to be solved at each split throughout all possible values of tested descriptors. A block diagram illustrating the process is shown in Fig. 6. A typical decision tree built on a database of around 200 B-Scans for scenes

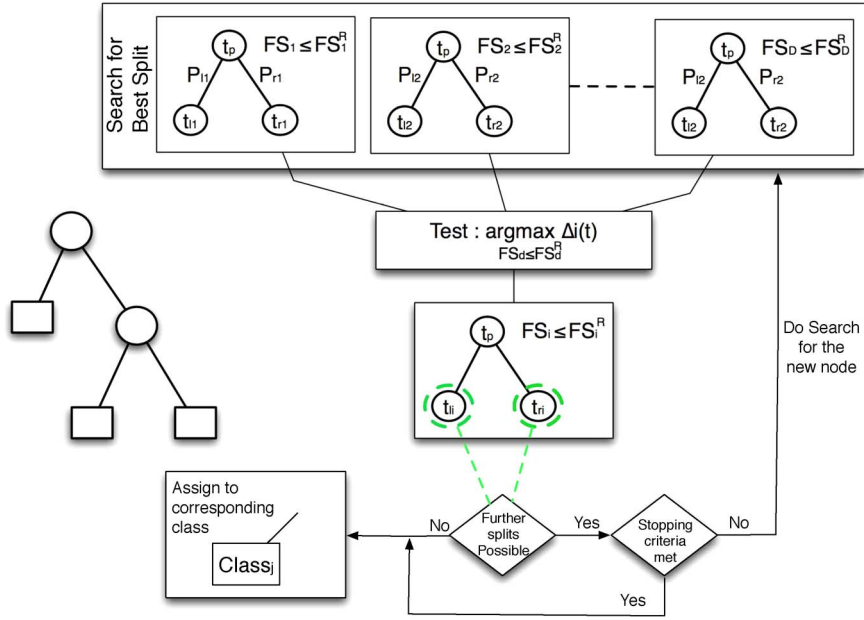


Fig. 6. Decision tree growing process.

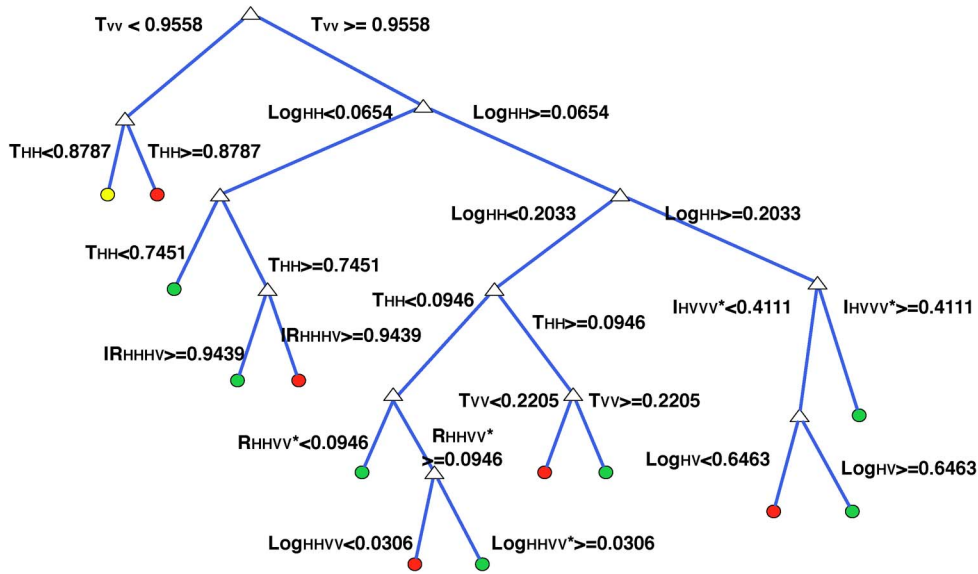


Fig. 7. Typical decision tree for one-target scene. Yellow dots are for the noise class. Red is for the clutter class, and green is for the target class.

that contain one target (different types of targets) is shown in Fig. 7. The major drawback, however, is that decision trees usually have relatively low prediction accuracy [57]. One of the best ways to improve the performance of decision tree-based algorithms is to use ensembles of trees [60] and random forests are one of the methods to enhance performance [31], [57].

A random forest is an ensemble of trees $T_0(\mathbf{FS}), \dots, T_{B-1}(\mathbf{FS})$, where \mathbf{FS} is the D -dimensional vector of features or descriptors associated with a superpixel (or with a cluster if clustering is used) and B is the number of trees in the ensemble. The ensemble produces B outputs $\hat{O}_0, \hat{O}_1, \dots, \hat{O}_{B-1}$ where \hat{O}_b is the prediction by the b th tree and $b = 0, 1, \dots, B - 1$. Outputs of all trees are aggregated to produce one final prediction, \hat{O} which is the class predicted by the majority of trees. Given data on a set of N superpixels for training, $\chi = (\mathbf{FS}_0, O_0), \dots, (\mathbf{FS}_{N-1}, O_{N-1})$, where \mathbf{FS}_n is a vector of

descriptors and O_n is the corresponding class label. Then, the following steps are implemented for training.

- 1) From N superpixels as training data, randomly sample, with replacement (bootstrap [61]), to create B bootstrap samples (same number of trees).
- 2) For each bootstrap sample, grow a decision tree using only α randomly selected features to test for best splitting at each node (rather than all features). The tree is grown to the maximum size (until no further splits are possible) and not pruned back.

A typical block diagram illustrating the training and testing process using random forest is shown in Fig. 8. Random forests performs a type of cross-validation in parallel with the training step by using out-of-bag (OOB) samples [62]. Specifically, in the process of training, each tree is grown using a bootstrap

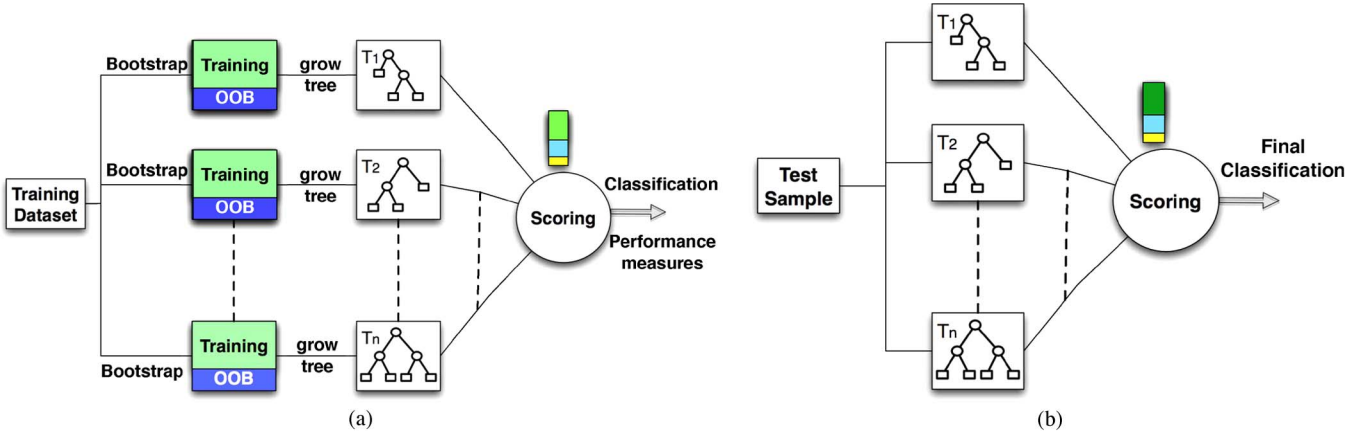


Fig. 8. Random forests training and testing process. (a) Training process. (b) Testing process.

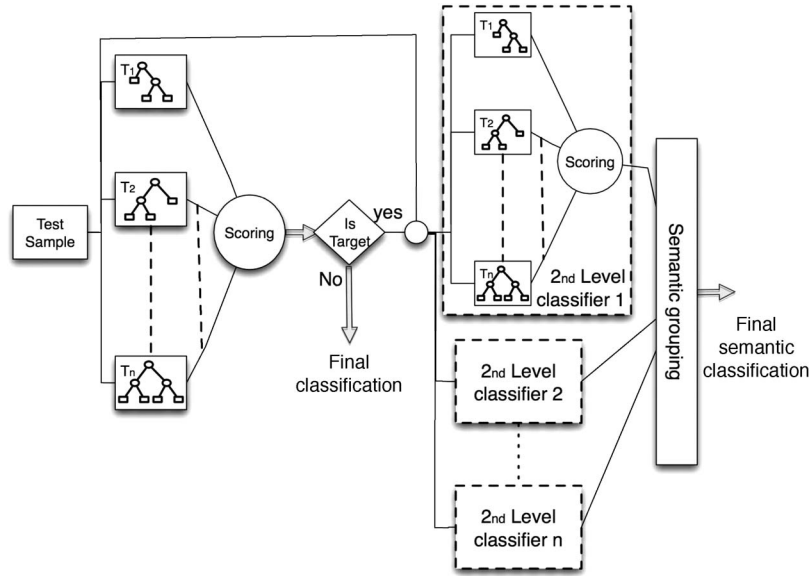


Fig. 9. Block diagram for the multilevel classifier.

sample. Since bootstrapping is sampling with replacement from the training data, some of the superpixels will not be included, while others will be repeated on each sample. The superpixel samples that were not included are called “OOB” samples. Usually, each tree is grown using two-thirds of the training data, and one-third is the OOB samples. These OOB samples can be used to estimate the ensemble prediction performance by testing the b th tree T_b against χ_b^{OOB} and calculating the classification error as follows:

$$ER \approx ER^{OOB} = \frac{\sum_{i=1}^l I(\hat{O}^{OOB}(\mathbf{FS}_i) \neq O_i)}{l} \quad (22)$$

where $I(\cdot)$ is an indicator function and l is the number of samples used [57]. A measure of how each feature contributes to the prediction accuracy can be calculated in the training process too. When a feature is “noised up” (e.g., replaced with random noise), the accuracy of prediction should noticeably degrade if the feature contributes to the prediction accuracy. On the other hand, it should have little effect on the performance if it is irrelevant. In classification, the change in prediction accuracy is usually a less sensitive measure than the change in

the margin. The margin is the difference between the proportion of votes for the correct class and the maximum of the proportion of votes for the incorrect classes. The tendency of the margin to become smaller (more negative or less positive) when a feature is “noised up” is what is used to assess the feature importance in classification [57].

The feature importance is calculated as follows: use the χ_b^{OOB} to make predictions of the b th tree when this tree is grown. At the same time, each feature in the χ_b^{OOB} data is randomly permuted, one at a time, and predicted by the tree. At the end of the training process, the margins for each class are calculated based on both the original OOB and the OOB data with each feature permuted. Then, the measure of importance for the d th feature is simply $\beta - \beta_d$, where β is the average margin based on the OOB prediction and β_d is the average margin based on the OOB prediction with the d th feature permuted.

After calculating the features importance, a new ensemble of trees is built upon the most contributing features only. This can be used to build different ensembles according to the classes needed, for example, an ensemble can be built to discriminate between target and nontarget superpixels. Another one can be built to discriminate between metal and nonmetal targets, or

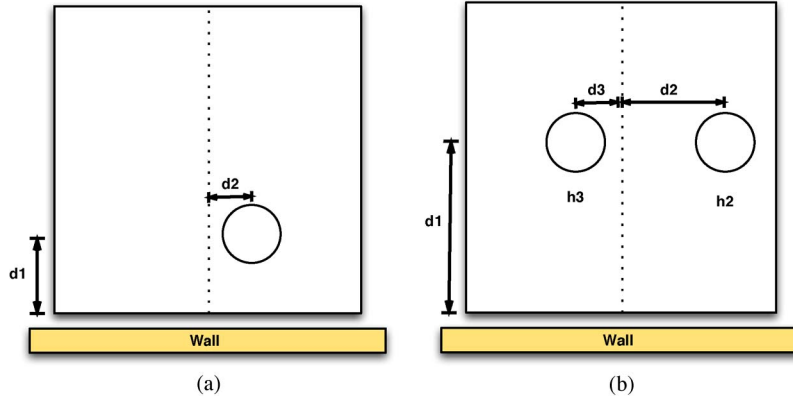


Fig. 10. Experiment diagram for one-target and two-target scenes. (a) One target, $d1 = 21.81$ in and $d2 = 11.26$ in at height = 47.5 in. (b) Two targets, $d2 = 42.26$ in, $d3 = 4.74$ in, $h2 = 39$ in, and $h3 = 47.5$ in.

TABLE II
SEGMENTATION BY CLASSIFICATION ALGORITHM STEPS

No.	Step
1	Prepare polarimetric images. A set of B-scans for each polarization. Each B-Scan has Q pixels.
2	Extract feature vector F_q with D features for each pixel q .
5	Generate S super-pixels for each B-scan using quick shift segmentation.
4	Generate Feature vector $F S_s$ for each super-pixel s using the underlying pixels features.
5	Prepare training and testing data for classification.
6	Do preparatory training for Random forests to choose best number of features for splitting and most important features.
7	build RF classifier with these parameters.
8	Repeat for different purpose classifiers (target or not, human or not, metal or not, ..etc) and arrange in multi-level scheme.

between “dihedral, sphere, and trihedral” classes. This may require additional types of features like shape features for example, but in this paper, we restrict ourselves to polarimetric features only. These ensembles could be used sequentially or in parallel or have mixed architectures. A proposed scheme for the sequential classifier is shown in Fig. 9. The decisions for each classifier could be semantically grouped to provide better understanding about the target. Furthermore, a third level could be added on the scheme provided on Fig. 9 to deal with the 3-D image directly, which could make use of geometrical and shape features to add more information about the targets detected.

VII. EXPERIMENTAL RESULTS

The imaging system used throughout this paper is a synthetic aperture radar system [63], where a single horn antenna, in motion, synthesizes a 57×57 element planar array. The interelement spacing is 0.875 in. The array standoff distance from the wall is 41.5 in. As described above, a continuous-wave stepped-frequency signal is used to approximate a wideband pulse. The experimental setup is shown in Fig. 10, which involves two experiments. The first experiment involves one target from the following: metal dihedral, metal sphere, metal trihedral, and a salt water jug placed at height of 47.5 in. The second experiment involves two targets in two arrangements, the first includes two dihedrals, and the second includes a metal sphere and a salt water jug at two different heights 39 in and 47.5 in. The targets are placed on a high foam column behind a concrete wall of thickness 5.622 in.

We consider the scenario presented in Section II for evaluation of the proposed techniques. As mentioned, we have four “one-target” 3-D images and 2 “two-target” 3-D images, each 3-D image is constructed from a set of 57 2-D B-scans. Each of these images has three different polarization data images, “HH, HV, and VV,” resulting in 18 different sets. Our experiments are arranged as follows (a summary is given in Table II).

- (a) Prepare the polarimetric data of the images.
- (b) Get the polarimetric features or signatures for the images. Each pixel will have a vector of 19 features as mentioned in Section III.
- (c) The feature matrix should be checked for outliers and scaled so as to avoid unexpected behavior.
- (d) Use Quickshift to segment the images based on the polarimetric features. Each image will be segmented to regions called superpixels as shown in Fig. 4.
- (e) Clean the resulting superpixels by removing superpixels that contain only one pixel.
- (f) For each superpixel, get the median of the feature vectors of all the superpixels contained on this superpixel. This will be the new feature vector for this superpixel as mentioned in Section IV.
- (g) Optionally use clustering if the number of the superpixels is large or the number of superpixels that contain noise and clutter classes is much larger than superpixels that contain target class as mentioned in Section V. If clustering is used, then again a median feature vector should be generated for each cluster based on the superpixels contained on this cluster.

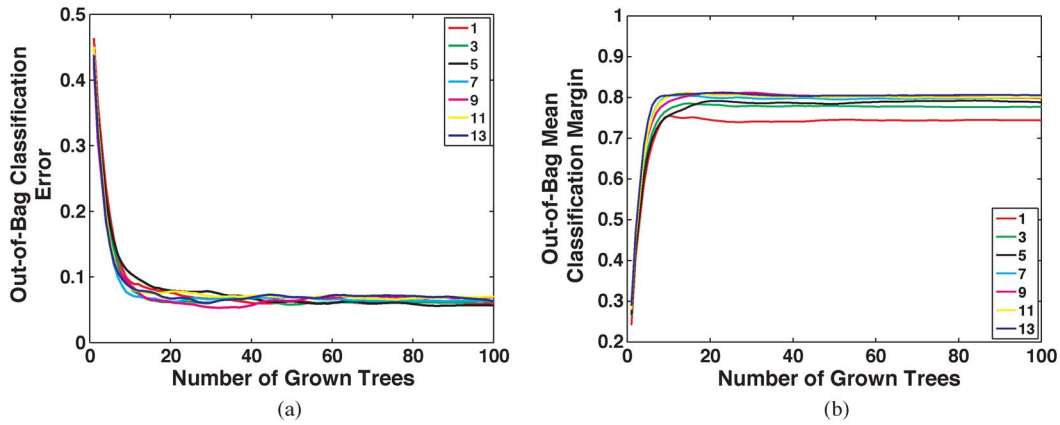


Fig. 11. Test for the suitable number of random features to be tested at each split. Left is the OOB classification error, and the right is the OOB classification margin, both versus the number of grown trees. Ensembles are trained on mixed data.

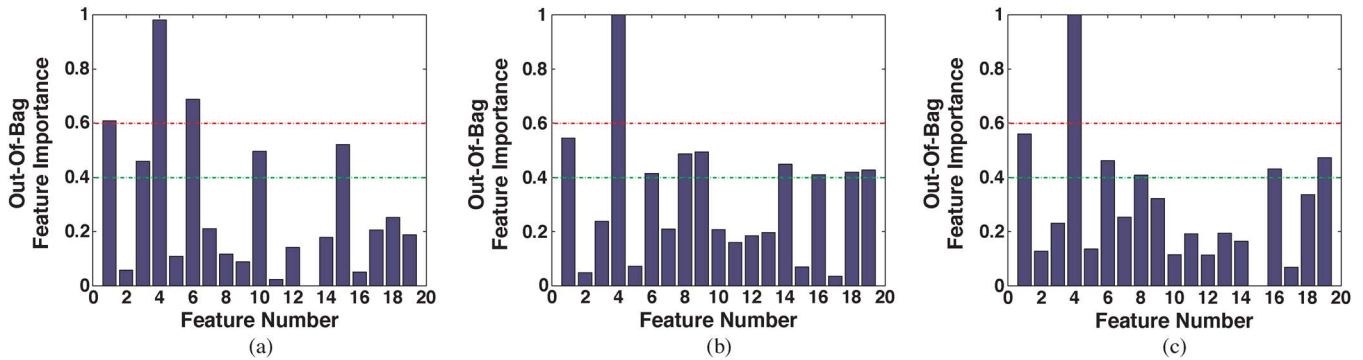


Fig. 12. Test for feature importance for classifying “target,” “clutter,” and “noise” classes, the green and red line are just guide lines for the features with feature importance more than 0.4 and 0.6, respectively. (a) is for ensemble trained on “one target” data, (b) is for ensemble trained on “two target” data, and (c) is for ensemble trained on mixed data.

- (h) Separate the data to training and testing sets. The training set is two-thirds, and the testing set is one-third of the data.
- (i) Prepare three training data groups. The first uses the “one target data,” the second the “two target” data, and the third is a mixed group between one and two target data and two testing data groups based on “one-target” and “two-target” data.
- (j) Use the training data to train the first ensemble of trees to classify between noise, clutter, and target classes. Subsequently rebuild the ensemble using the most affecting features only.
- (k) The previous step should be repeated for the three groups of training data to create three different ensembles.
- (l) The last steps are repeated to build two other groups of ensembles. The first classifies between generic “metal” and “nonmetal” classes, and the second classifies between the target types “dihedral,” “sphere,” “trihedral,” and “salt-water jug.”

The first ensemble of 100 trees is trained to classify between three classes (“noise,” “clutter,” and “target”), with all the features used. As mentioned before, three different ensembles depending on the training data (“one target,” “two target,” and “mixed”) are grown. We first need to choose the number of features that will be randomly tested for best split at each tree node. The usual number is the round up of the square root of the number of features (which in our case is 5). We conducted dif-

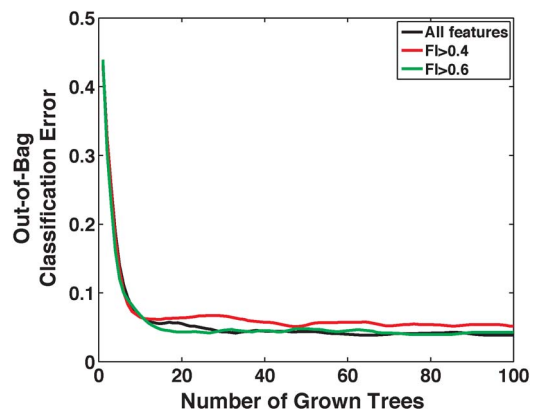


Fig. 13. OOB classification error for reduced feature set compared to using all features.

ferent experiments to choose the optimum number of features tested for split using the numbers = [1, 3, 5, 7, 9, 11, 13] as candidates. Both the classification error and the mean classification margin against the number of grown trees have been checked. The number of features that gave the lowest OOB classification error and best mean classification margin is used. Fig. 11 shows the OOB classification error and the mean classification margin for the three ensembles. The lowest classification error is gained when using 3, 5, 7, and 13 random features at each split on the different ensembles, and among these numbers, the number of

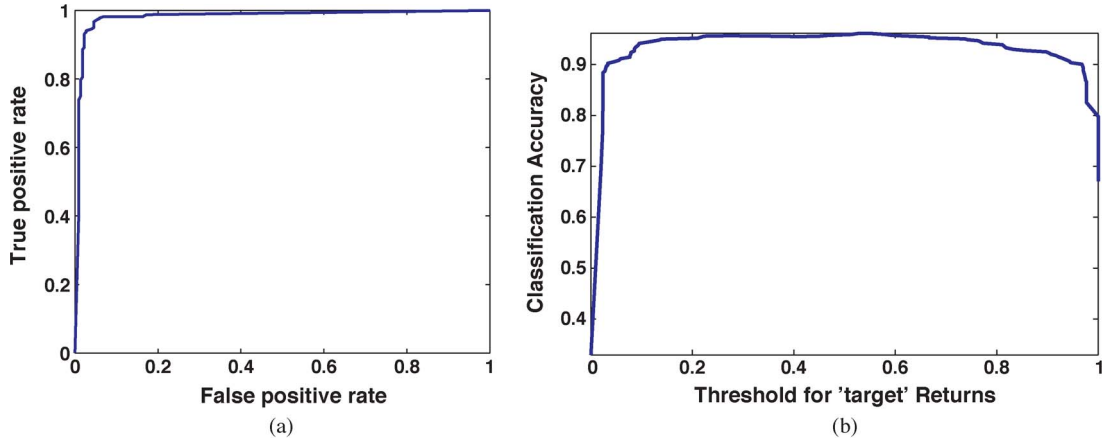


Fig. 14. ROC curve and classification accuracy for a reduced feature set. (a) Standard ROC. (b) Classification accuracy versus “target” return threshold.

TABLE III
PERFORMANCE MEASURES FOR THE FIRST ENSEMBLE USING OOB SAMPLES, CLASSIFYING “TARGET,” “NOISE,” AND “CLUTTER” CLASSES

Training	Measure	AUC	Optimal threshold	Optimal operating point
one target		0.9887	0.45	(0.0486, 0.9753)
two targets		0.9896	0.5279	(0.0280, 0.9247)
mixed		0.9878	0.406	(0.0668, 0.9685)

features that resulted in the highest mean classification margin is chosen for each case. Thus, seven features for the case of “one target” data and five features for the other two cases are chosen for testing for best split. To estimate the feature importance, features are permuted and tested as mentioned in Section VI. The results are shown in Fig. 12. As can be seen, the six most important features for the ensemble trained with “one target” data are [1, 3, 4, 6, 10, 15], which are: the thresholded intensity for HH (T_{HH}), the thresholded intensity for VV (T_{VV}), the logarithmic intensity for HH (\log_{HH}), the logarithmic intensity for VV (\log_{VV}), and the imaginary part of the product of HH and HV* (Im_{HHHV^*}). The features with an importance above 0.6 are [1, 4, 6]. A comparison between the OOB classification error for both the reduced feature sets and the set with all features is shown in Fig. 13, which shows no significant degradation in performance for both of the reduced feature sets. Thus, a feature set of the six most important features will be used. Table IX lists the most important features for each case.

Performance curves for the reduced feature set for the ensemble trained on “one-target” data are shown in Fig. 14. The left curve depicts the false positive rate against the true positive rate. The curve has 0.9887 as the area under the curve (AUC) and an optimal operating point at (0.0486, 0.9753). The right curve is the ensemble accuracy versus threshold on the score for the “target” class. The curve shows a flat region indicating that any threshold from 0.3 to 0.6 is a reasonable choice. Calculating the maximum accuracy shows that it is achieved at a threshold around 0.45. Table III lists the AUC, the optimal operating point, and the optimal threshold for all cases.

Testing the different ensembles of trees, which was trained using samples from the “one-target,” “two-target,” and “mixed” data with both the “one target” data and the “two target” data

TABLE IV
CLASSIFICATION ERRORS FOR THE FIRST ENSEMBLE, CLASSIFYING “TARGET,” “NOISE,” AND “CLUTTER” CLASSES. SEGMENTATION BY CLASSIFICATION, AND MAHALANOBIS DISTANCE CLASSIFIER (USING ICM AND LSM SEGMENTATION METHODS) ARE COMPARED

Testing	Training	Seg. by Class.			ICM			LSM		
		one target	two target	mixed	one target	two target	mixed	one target	two target	mixed
one target	one target	0.043	0.116	0.0429	0.063	0.176	0.0735	0.0763	0.2263	0.1093
two targets	two targets	0.139	0.072	0.0389	0.343	0.0763	0.0459	0.3433	0.2216	0.0863

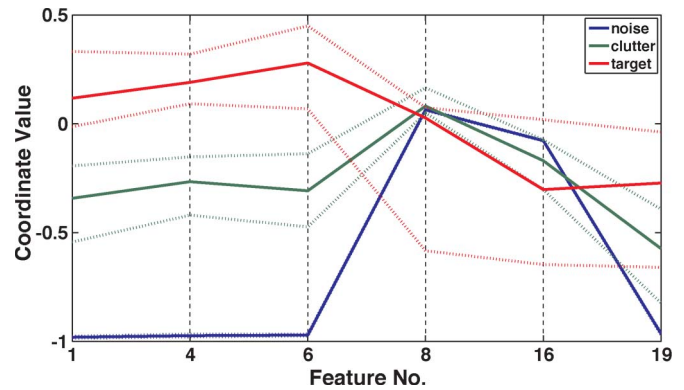


Fig. 15. Parallel co-ordinates plot for the distance between the different classes using mixed training data.

gives a classification error between 0.04–0.072 for matched cases, around 0.1 for the mismatched case, and between 0.03–0.043 for the mixed training case. The classification error for all cases is listed in Table IV in comparison to Mahalanobis distance classifier (using ICM and levelset (LSM) segmentation methods) [30].

Fig. 15 demonstrates the distance between the “target,” “noise,” and “clutter” classes using the most affecting features for the ensemble trained with mixed data. The three lines for each class represent the median and quantiles at 0.1 and 0.9 of the observations. It is clear that the first three features discriminate well between the different classes and the other features could help tuning after the different tree splits. Repeating the previous experiments changing the classification objective as mentioned before, i.e., we first discriminate between the classes “metal” and “nonmetal” and then between the classes “dihedral,” “sphere,” “triangular,” and “salt water jug” shows

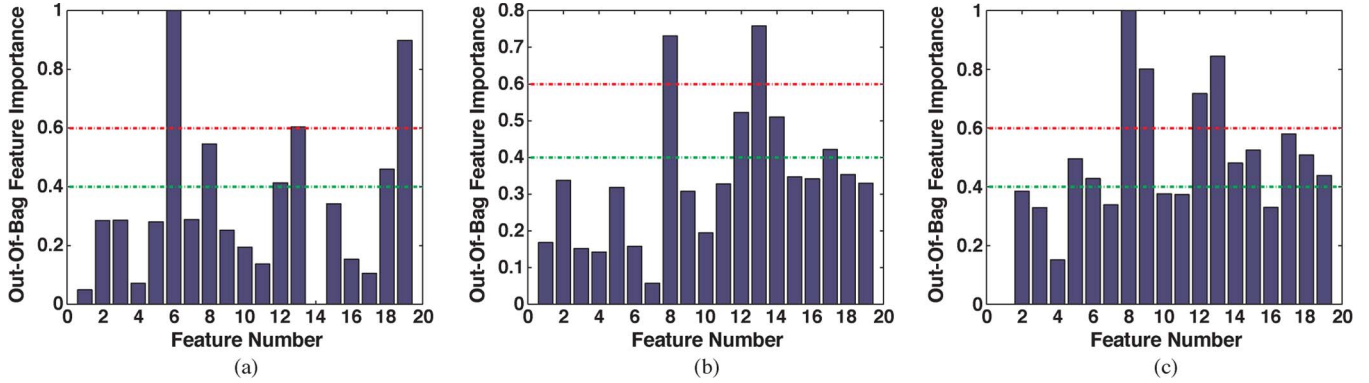


Fig. 16. Test for feature importance for classifying metal targets, the green and red lines are just guide lines for the features with feature importance more than 0.4 and 0.6, respectively. (a) is for ensemble trained on “one-target” data, (b) is for ensemble trained on “two-target” data, and (c) is for ensemble trained on mixed data.

TABLE V
PERFORMANCE MEASURES FOR THE SECOND ENSEMBLE USING OOB SAMPLES, CLASSIFYING METAL TARGET CLASS

Training \ Measure	AUC	Optimal threshold	Optimal operating point
one target	1	0.589	(0, 1)
two targets	0.9995	0.6304	(0.027, 1)
mixed	0.9873	0.55	(0.0462, 0.9947)

TABLE VI
CLASSIFICATION ERROR FOR THE SECOND ENSEMBLE, CLASSIFYING A METAL TARGET CLASS. SEGMENTATION BY CLASSIFICATION, AND MAHALANOBIS DISTANCE CLASSIFIER (USING ICM AND LSM SEGMENTATION METHODS) ARE COMPARED

Testing \ Training	Seg. by Class.			ICM			LSM		
	one target	two target	mixed	one target	two target	mixed	one target	two target	mixed
one target	0.037	0.2593	0.0556	0.6432	0.7584	0.7126	0.5335	0.8522	0.7126
two targets	0.2329	0	0	0.8334	0.6354	0.6635	0.7639	0.4698	0.5646

that the proposed scheme can be used for such a classification task. Fig. 16 shows the feature importance when classifying for metal targets. Table V lists the AUC, the optimal operating point and the optimal threshold for this case. Testing the different ensembles of trees which was trained using samples from the “one-target,” “two-target,” and “mixed” data with both the “one-target” data and the “two-target” data gives a classification error between 0–0.037 for matched cases, around 0.2 for the mismatched case, and between 0–0.0556 for the mixed training case. The classification error for all cases is listed in Table VI in comparison to Mahalanobis distance classifier (using ICM and LSM segmentation methods).

It is worth noting that the classification error is much higher in mismatched cases (where training is based on one-target data and testing is used with two-target data and vice-versa), which implies a significant change in the features when other targets are present.

Fig. 17 shows the feature importance when classifying target types. Table VII lists the AUC, the optimal operating point, and the optimal threshold for this case. Testing this case gives a classification error between 0 and 0.1429 for matched cases, between 0.3 and 0.94 for mismatched cases, and between 0 and 0.14 for the mixed training case. The classification error for all cases is listed in Table VIII in comparison to Mahalanobis distance classifier (using ICM and LSM segmentation methods).

Table IX lists the important features regarding each built ensemble, the most important feature has the symbol “■” and the features belonging to the six most important features are marked with “▲”.

The features that were generally significant are [1, 4, 6, 8, 9, 12, 13, 19], which represent features from all the main feature types mentioned in Section III. It is also worth noting that all of them are derived from HH and VV polarizations except for feature 19, the even bounce energy. Also, feature 8 (\log_{PHHV}) which is the logarithmic phase between HH and VV polarizations is an important feature in mostly all the trained ensembles. Most important features that affected classifying between “target,” “clutter,” and “noise” classes are [1, 4, 8, 19] and the most important one in this case, which is feature 4, are derived from the HH polarization, like feature 1. For the metal target classification, the most important features are [6, 8, 12, 13, 15, 17], we see that features 15 (Im_{HHV^*}) and 17 (Im_{HVV^*}) are excellent features in this case. They both involve the HV polarization, and they were not so important for “target,” “clutter,” and “noise” classification. For the target types classification, we can see that feature 12 (Re_{HHV^*}) is the most important feature for all the trained ensembles on this case. Fig. 18 shows the final segmentation and classification result for the first ensemble group that classified between “target,” “clutter,” and “noise” classes using segmentation by classification compared to segmentation using ICM and LSM. The segmented scene contained two metal dihedrals at the same distance from the platform and at different heights. It can be seen from the figure that using simple segmentation methods depending only on pixel intensity was able to get the real positions of the targets, but it suffered from ghost targets as in the case of ICM or from large false positive detections as in the case of LSM. Taking into account that the three algorithms have the same initial pixel intensity threshold to begin with, segmentation by classification has better segmentation results than the other algorithms.

VIII. CONCLUSION

The problem of target segmentation and classification in the image domain with application to TWRI has been addressed. We have overcome the limitations of algorithms based on a pixel-grid, which is not a natural representation of visual

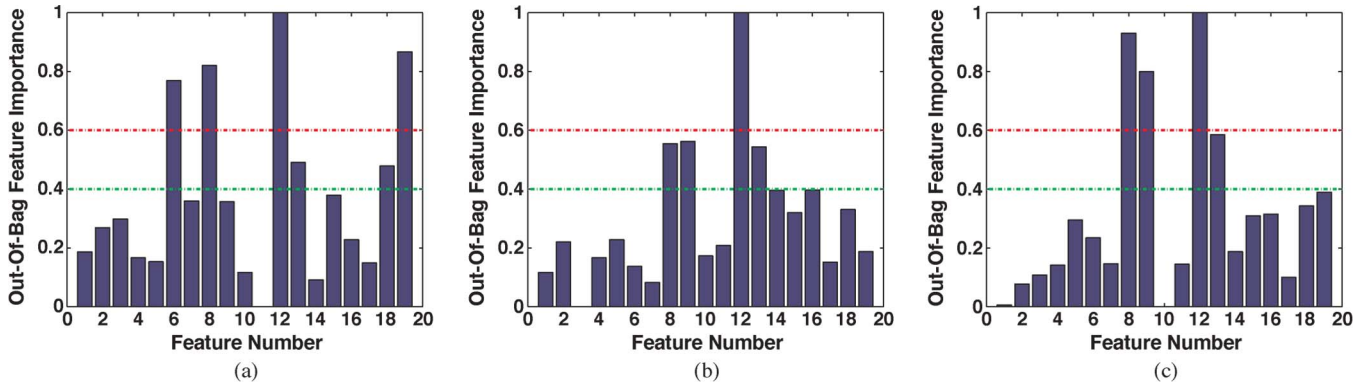


Fig. 17. Test for feature importance for classifying target types, the green and red lines are just guide lines for the features with feature importance more than 0.4 and 0.6, respectively. (a) is for ensemble trained on “one target” data, (b) is for ensemble trained on “two target” data, and (c) is for ensemble trained on mixed data.

TABLE VII
PERFORMANCE MEASURES FOR THE THIRD ENSEMBLE USING OOB SAMPLES, CLASSIFYING TARGET TYPES CLASSES

Training		Measure	AUC	Optimal threshold	Optimal operating point
dihedral	one target		0.9988	0.7917	(0, 0.9394)
	two targets		1	0.8333	(0, 1)
	mixed		0.9993	0.6579	(0.0073, 0.9915)
sphere	one target		0.9984	0.444	(0.013, 0.9697)
	two targets		0.9997	0.8286	(0, 0.96)
	mixed		0.9954	0.5714	(0.0152, 0.9828)
trihedral	one target		0.9970	0.7813	(0.01, 0.928)
	two targets		—	—	—
	mixed		0.9967	0.5135	(0, 0.9286)
saltwater jug	one target		0.9996	0.6857	(0, 0.9643)
	two targets		0.9988	0.675	(0, 0.973)
	mixed		0.9956	0.6071	(0, 0.9385)

TABLE VIII
CLASSIFICATION ERROR FOR THE THIRD ENSEMBLE, SEGMENTATION BY CLASSIFICATION, AND MAHALANOBIS DISTANCE CLASSIFIER (USING ICM AND LSM SEGMENTATION METHODS) ARE COMPARED

Testing \ Training		Seg. by Class.			ICM			LSM		
		one target	two target	mixed	one target	two target	mixed	one target	two target	mixed
dihedral	one target	0	0	0	0.352	0.432	0.214	0.354	0.514	0.5167
	two targets	0	0	0	0.626	0.3176	0.312	0.554	0.421	0.621
sphere	one target	0.1176	0.705	0.0588	0.475	0.8864	0.426	0.2841	0.878	0.3365
	two targets	0.3846	0	0	0.6276	0.3243	0.2116	0.5543	0.3236	0.4452
trihedral	one target	0	—	0	0.5447	—	0.3447	0.2332	—	0.2332
	two targets	—	—	—	—	—	—	—	—	—
saltwater jug	one target	0.1429	0.0714	0.1429	0.3632	0.4854	0.4362	0.2782	0.5321	0.4325
	two targets	0.9444	0	0	0.6387	0.3154	0.2543	0.8854	0.366	0.4265
overall	one target	0.0741	0.3704	0.0556	0.4337	0.6017	0.355	0.2873	0.6417	0.3795
	two targets	0.3014	0	0	0.6307	0.3191	0.2593	0.6645	0.3702	0.4977

TABLE IX
FEATURE IMPORTANCE FOR EACH BUILT ENSEMBLE

Classify	Built on	features																		
		1	2	3	4	5	6	7	8	9	10	11	12	13	14	15	16	17	18	19
Target or not	1 target	▲		▲	■		▲			▲						▲				
	2 targets	▲			■			▲	▲						▲					▲
	mixed	▲			■		▲		▲									▲		▲
Metal or not	1 target						■		▲				▲	▲		▲				▲
	2 targets								▲				▲	■	▲				▲	▲
	mixed								■	▲			▲	▲		▲			▲	▲
Target types	1 target						▲		▲				■	▲					▲	▲
	2 targets								▲	▲			■	▲	▲		▲			
	mixed								▲	▲			■	▲					▲	▲

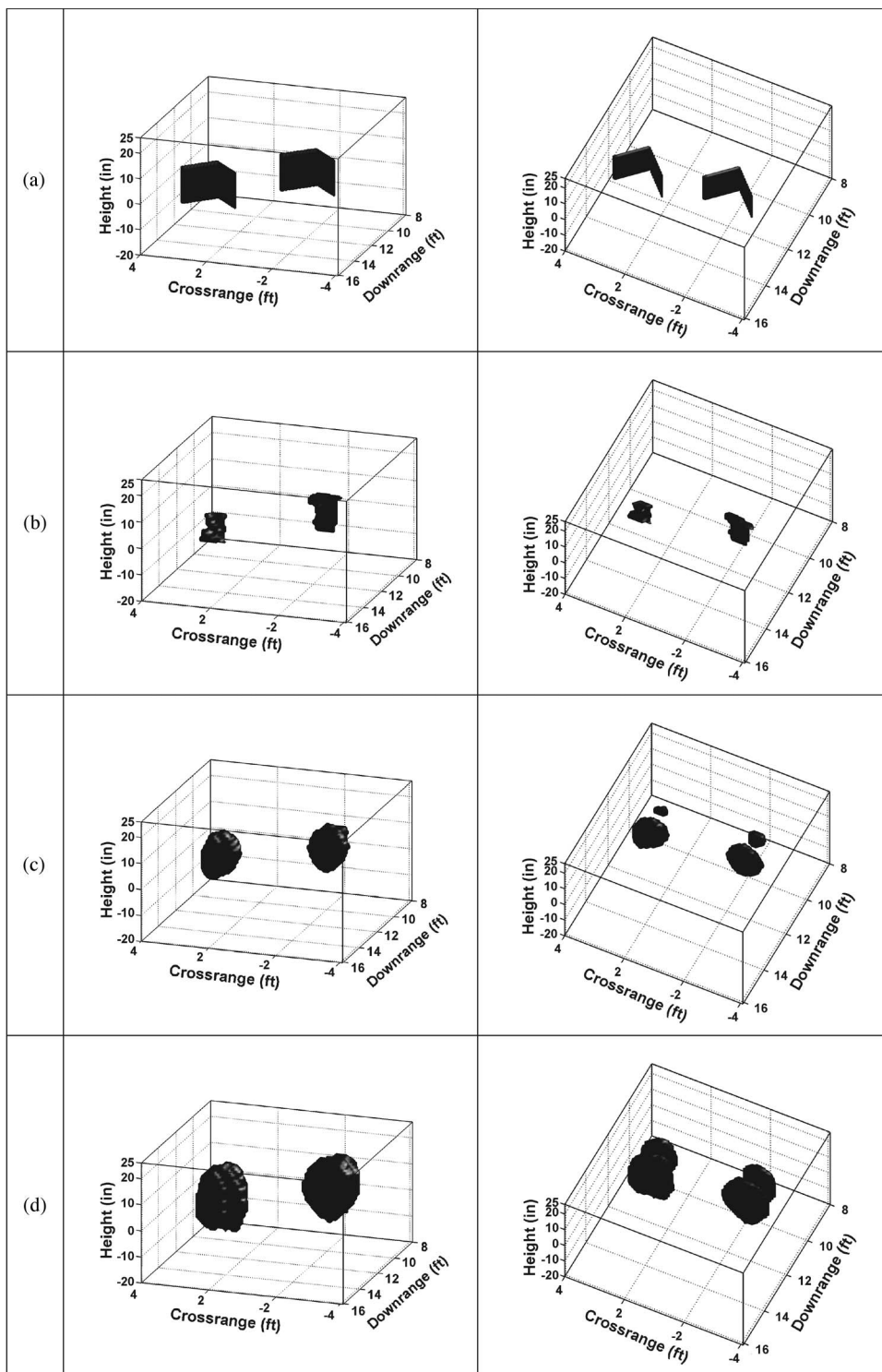


Fig. 18. Front and top views of final 3-D segmentation of a two target scene containing two dihedrals. (a) Original scene. (b) Segmentation by classification. (c) ICM. (d) LSM.

scenes. Perceptually meaningful entities, obtained from a low-level grouping process, the so-called superpixels are considered in this paper. Further, simple geometrical and statistical descriptors that have been used as features in the past are extended to polarimetric descriptors, which make use of the whole polarimetric information in radar images. A framework of polarimetric feature extraction, oversegmentation (superpixels), clustering, and classification has been presented. An

expandable sequential classifier based on random forests has been proposed to discriminate targets from clutter returns and to provide further information about the discriminated targets. The experimental results demonstrate the usefulness of the proposed methods as desired target returns are discriminable from clutter returns and a further classification about target type and its nature is provided. The proposed technique proved better performance than techniques that depends only on pixel intensity.

ACKNOWLEDGMENT

The Authors wish to thank Prof. Dr. Moeness G. Amin and Dr. Fauzia Ahmad from the Center of Advanced Communication at Villanova University for providing the real data.

REFERENCES

- [1] M. G. Amin, Ed., *Through-the-Wall Radar Imaging*. Boca Raton, FL: CRC Press, 2011.
- [2] D. D. Ferris and N. C. Currie, "A survey of current technologies for through-the-wall surveillance TWS," in *Proc. SPIE Conf. Sensors, C31 Inf., Training Technol. Law Enforcement*, Boston, MA, 1998, vol. 3577, pp. 62–72.
- [3] M. Amin and K. Sarabandi, "Special issue on remote sensing of building interior," *IEEE Trans. Geosci. Remote Sens.*, vol. 47, no. 5, pp. 1267–1268, May 2009.
- [4] "Special issue: Advances in indoor radar imaging," *J. Franklin Inst.*, vol. 345, no. 6, pp. 556–722, 2008.
- [5] C. Debes, M. G. Amin, and A. M. Zoubir, "Target detection in single- and multiple-view through-the-wall radar imaging," *IEEE Trans. Geosci. Remote Sens.*, vol. 47, no. 5, pp. 1349–1361, May 2009.
- [6] E. Baranoski, "Through-wall imaging: Historical perspective and future directions," *J. Franklin Inst.*, vol. 345, no. 6, pp. 556–569, Sep. 2008.
- [7] P. Setlur, M. Amin, and F. Ahmad, "Multipath model and exploitation in through-the-wall and urban radar sensing," *IEEE Trans. Geosci. Remote Sens.*, vol. 49, no. 10, pp. 4021–4034, Oct. 2011.
- [8] R. Solimene, F. Soldovieri, G. Prisco, and R. Pierri, "Three-dimensional through-wall imaging under ambiguous wall parameters," *IEEE Trans. Geosci. Remote Sens.*, vol. 47, no. 5, pp. 1310–1317, May 2009.
- [9] R. Solimene, R. Di Napoli, F. Soldovieri, and R. Pierri, "TWI for an unknown symmetric lossless wall," *IEEE Trans. Geosci. Remote Sens.*, vol. 49, no. 8, pp. 2876–2886, Aug. 2011.
- [10] F. Ahmad and M. Amin, "Noncoherent approach to through-the-wall radar localization," *IEEE Trans. Aerosp. Electron. Syst.*, vol. 42, no. 4, pp. 1405–1419, Oct. 2006.
- [11] F. Ahmad and M. Amin, "Multi-location wideband synthetic aperture imaging for urban sensing applications," *J. Franklin Inst.*, vol. 345, no. 6, pp. 618–639, Sep. 2008.
- [12] M. Dehmollaian and K. Sarabandi, "Through-the-wall imaging: Measurement and modeling techniques," presented at the Proc. IEEE Int. Geoscience Remote Sensing Symp., Boston, MA, 2008, Paper THP.Z.7.
- [13] Y.-S. Yoon and M. G. Amin, "High-resolution through-the-wall radar imaging using beamspace music," *IEEE Trans. Antennas Propag.*, vol. 56, no. 6, pp. 1763–1774, Jun. 2008.
- [14] T. Dogaru and C. Le, "SAR images of rooms and buildings based on FDTD computer models," *IEEE Trans. Geosci. Remote Sens.*, vol. 47, no. 5, pp. 1388–1401, May 2009.
- [15] R. Narayanan, "Through-wall radar imaging using UWB noise waveforms," *J. Franklin Inst.*, vol. 345, no. 6, pp. 659–678, Sep. 2008.
- [16] C.-P. Lai and R. M. Narayanan, "Ultrawideband random noise radar design for through-wall surveillance," *IEEE Trans. Aerosp. Electron. Syst.*, vol. 46, no. 4, pp. 1716–1730, Oct. 2010.
- [17] H. Estephan, M. G. Amin, and K. M. Yemelyanov, "Optimal waveform design for improved indoor target detection in sensing through-the-wall applications," *IEEE Trans. Geosci. Remote Sens.*, vol. 48, no. 7, pp. 2930–2941, Jul. 2010.
- [18] F. Ahmad and M. G. Amin, "Matched-illumination waveform design for a multistatic through-the-wall radar system," *IEEE J. Sel. Topics Signal Process.*, vol. 4, no. 1, pp. 177–186, Feb. 2010.
- [19] C. Debes, J. Riedler, M. G. Amin, and A. M. Zoubir, "Iterative target detection approach for through-the-wall radar imaging," in *Proc. IEEE ICASSP*, Apr. 2009, pp. 3061–3064.
- [20] C. Debes, J. Hahn, M. G. Amin, and A. M. Zoubir, "Feature extraction in through-the-wall radar imaging," in *Proc. IEEE Int. Conf. Acoust., Speech, Signal Process.*, 2010, pp. 3562–3565.
- [21] C. Debes, C. Weiss, M. G. Amin, and A. M. Zoubir, "Distributed target detection in through-the-wall radar imaging using the bootstrap," in *Proc. IEEE Int. Conf. Acoust., Speech, Signal Process.*, 2010, pp. 3530–3533.
- [22] C. Debes, J. Riedler, M. G. Amin, and A. M. Zoubir, "Adaptive target detection with application to through-the-wall radar imaging," *IEEE Trans. Signal Process.*, vol. 58, no. 11, pp. 5572–5583, Nov. 2010.
- [23] C. Debes, A. M. Zoubir, and M. G. Amin, "Optimal decision fusion in through-the-wall radar imaging," in *Proc. IEEE Int. Workshop Stat. Signal Process.*, 2009, pp. 761–764.
- [24] F. Ahmad and M. G. Amin, "Through-the-wall polarimetric imaging," in *Proc. SPIE—Algorithms Synthetic Aperture Radar Imagery XV*, 2008, vol. 6970, pp. 69700N-1–69700N-10.
- [25] Y. Wang, Y. Yang, and A. E. Fathy, "Experimental assessment of the cross coupling and polarization effects on ultra-wide band see-through-wall imaging reconstruction," in *Proc. IEEE MTT-S Int. Microw. Symp. Dig.*, 2009, pp. 9–12.
- [26] T. Dogaru and C. Le, "Through-the-wall small weapon detection based on polarimetric radar techniques," Army Res. Lab., Adelphi, MD, 2009, Tech. Rep. ARL-TR-5041.
- [27] K. M. Yemelyanov, N. Engheta, A. Hoorfar, and J. A. McVay, "Adaptive polarization contrast techniques for through-wall microwave imaging applications," *IEEE Trans. Geosci. Remote Sens.*, vol. 47, no. 5, pp. 1362–1374, May 2009.
- [28] M. Thiel and K. Sarabandi, "Ultra-wideband multi-static scattering analysis of human movement within buildings for the purpose of stand-off detection and localization," *IEEE Trans. Antennas Propag.*, vol. 59, no. 4, pp. 1261–1268, Apr. 2011.
- [29] C. Debes, A. M. Zoubir, and M. G. Amin, "Enhanced detection using target polarization signatures in through-the-wall radar imaging," *IEEE Trans. Geosci. Remote Sens.*, vol. 50, no. 5, pp. 1968–1979, May 2012.
- [30] C. Debes, J. Hahn, A. M. Zoubir, and M. G. Amin, "Target discrimination and classification in through-the-wall radar imaging," *IEEE Trans. Signal Process.*, vol. 59, no. 10, pp. 4664–4676, Oct. 2011.
- [31] L. Breiman, "Random forests," *Mach. Learn.*, vol. 45, no. 1, pp. 5–32, Oct. 2001.
- [32] C. Oliver and S. Quegan, *Understanding Synthetic Aperture Radar Images*. Raleigh, NC: SciTech, 2004.
- [33] J.-S. Lee and E. Pottier, *Polarimetric Radar Imaging, From Basics to Applications*, vol. 143, *Optical Science and Engineering*. Boca Raton, FL: CRC Press, Feb. 2009.
- [34] H. A. Zebker and J. J. Van Zyl, "Imaging radar polarimetry: A review," *Proc. IEEE*, vol. 79, no. 11, pp. 1583–1606, Nov. 1991.
- [35] S. R. Cloude and E. Pottier, "A review of target decomposition theorems in radar polarimetry," *IEEE Trans. Geosci. Remote Sens.*, vol. 34, no. 2, pp. 498–518, Mar. 1996.
- [36] P. Yu, A. K. Qin, and D. A. Clausi, "Unsupervised polarimetric SAR image segmentation and classification using region growing with edge penalty," *IEEE Trans. Geosci. Remote Sens.*, vol. 50, no. 4, pp. 1302–1317, Apr. 2012.
- [37] G. Zhou, Y. Cui, Y. Chen, J. Yang, H. Rashvand, and Y. Yamaguchi, "Linear feature detection in polarimetric SAR images," *IEEE Trans. Geosci. Remote Sens.*, vol. 49, no. 4, pp. 1453–1463, Apr. 2011.
- [38] R. Paladini, M. Martorella, and F. Berizzi, "Classification of man-made targets via invariant coherency-matrix eigenvector decomposition of polarimetric SAR/ISAR images," *IEEE Trans. Geosci. Remote Sens.*, vol. 49, no. 8, pp. 3022–3034, Aug. 2011.
- [39] J.-S. Lee, M. R. Grunes, and E. Pottier, "Quantitative comparison of classification capability: Fully polarimetric versus dual and single-polarization SAR," *IEEE Trans. Geosci. Remote Sens.*, vol. 39, no. 11, pp. 2343–2351, Nov. 2001.
- [40] J.-S. Lee, K. W. Hoppel, S. A. Mango, and A. R. Miller, "Intensity and phase statistics of multilook polarimetric and interferometric SAR imagery," *IEEE Trans. Geosci. Remote Sens.*, vol. 32, no. 5, pp. 1017–1028, Sep. 1994.
- [41] D. H. Hoekman and M. A. M. Vissers, "A new polarimetric classification approach evaluated for agricultural crops," *IEEE Trans. Geosci. Remote Sens.*, vol. 41, no. 12, pp. 2881–2889, Dec. 2003.
- [42] E. Rignot, R. Chellappa, and P. Dubois, "Unsupervised segmentation of polarimetric sar data using the covariance matrix," *IEEE Trans. Geosci. Remote Sens.*, vol. 30, no. 4, pp. 697–705, Jul. 1992.
- [43] A. A. Mostafa and A. M. Zoubir, "3d target detection in through-the-wall radar imaging," in *Proc. SPIE—Signal Processing, Sensor Fusion, Target Recognition XIX*, 2010, vol. 7697, p. 76971F.
- [44] D. E. Kreithen, S. S. Halversen, and G. J. Owirka, "Discriminating targets from clutter," *Lincoln Lab. J.*, vol. 6, no. 1, pp. 25–52, 1993.
- [45] X. Ren and J. Malik, "Learning a classification model for segmentation," in *Proc. 9th IEEE Int. Conf. Comput. Vis.*, 2003, vol. 1, pp. 10–17.
- [46] D. R. Thompson, L. Mandrake, M. S. Gilmore, and R. Castaño, "Superpixel endmember detection," *IEEE Trans. Geosci. Remote Sens.*, vol. 48, no. 11, pp. 4023–4033, Nov. 2010.
- [47] A. Vedaldi and S. Soatto, *Quick Shift and Kernel Methods for Mode Seeking*, vol. 5305, *Lecture Notes in Computer Science*. Berlin, Germany: Springer-Verlag, 2008, ch. 52, pp. 705–718.
- [48] B. Fulkerson, A. Vedaldi, and S. Soatto, "Class segmentation and object localization with superpixel neighborhoods," in *Proc. 12th IEEE Int. Conf. Comput. Vis.*, Sep. 2009, pp. 670–677.

[49] A. Vedaldi and B. Fulkerson, "VLFeat: An open and portable library of computer vision algorithms," in *Proc. ACM Multimedia*, 2010, pp. 1469–1472.

[50] R. O. Duda, P. E. Hart, and D. G. Stork, *Pattern Classification*, vol. 2. Hoboken, NJ: Wiley, 2001.

[51] T. Hastie, R. Tibshirani, and J. H. Friedman, *The Elements of Statistical Learning: Data Mining, Inference, and Prediction*. Berlin, Germany: Springer-Verlag, 2009.

[52] Z. Rosenbaum and B. G. Mobasseri, "Interpretation of through-the-wall radar imagery by probabilistic volume model building," in *Proc. SPIE—Defense, Security Sensing*, 2008, vol. 6943, pp. 69430T-1–69430T-10.

[53] B. G. Mobasseri and Z. Rosenbaum, "3D classification of through-the-wall radar images using statistical object models," in *Proc. IEEE Workshop Image Anal. Interpret.*, 2008, pp. 149–152.

[54] L. Breiman, J. H. Friedman, R. A. Olshen, and C. J. Stone, *Classification and Regression Trees*. Belmont, CA: Wadsworth, 1984.

[55] D. L. Verbyla, "Classification trees: A new discrimination tool," *Can. J. Forest Res.*, vol. 17, no. 9, pp. 1150–1152, Sep. 1987.

[56] L. A. Clark and D. Pregibon, *Tree-Based Models. Statistical Models in S*. Pacific Grove, CA: Wadsworth, 1992.

[57] V. Svetnik, A. Liaw, C. Tong, J. C. Culberson, R. P. Sheridan, and B. P. Feuston, "Random forest: A classification and regression tool for compound classification and qsar modeling," *J. Chem. Inf. Comput. Sci.*, vol. 43, no. 6, pp. 1947–1958, 2003.

[58] C. Gini, "Variability and mutability, contribution to the study of statistical distributions and relations," *Studi Economico-Giuridici della R. Università di Cagliari*, 1912.

[59] [Online: Stand 2011-05-23T08:37:58Z] R. Timofeev, Classification and Regression Trees(Cart) Theory and Applications2004, [Online: Stand 2011-05-23T08:37:58Z].

[60] T. G. Dietterich, *Ensemble Learning, Handbook of Brain Theory and Neural Networks*. Cambridge, MA: MIT Press, 2002.

[61] A. M. Zoubir and D. R. Iskander, *Bootstrap Techniques for Signal Processing*. Cambridge, U.K.: Cambridge Univ. Press, 2004.

[62] L. Breiman, "Out-of-bag estimation," Dept. Stat., UC Berkeley, Berkeley, CA, 1996, Tech. Rep..

[63] D. Massonnet and J.-C. Souyris, *Synthetic Aperture Radar Imaging*. Lausanne, Switzerland: EFPL Press, May 2008.



Christian Debes (S'06–M'11) received the M.Sc. and Dr.-Ing. degrees in electrical engineering from Technische Universität Darmstadt, Darmstadt, Germany, in 2006 and 2010, respectively.

He worked as a Postdoctoral Research Fellow in the Signal Processing Group, Technische Universität Darmstadt, from 2010 to 2011. In 2011, he joined the R&D Center of AGT Germany, Darmstadt, as a Senior Researcher in the area of sensor networks for urban management and environmental sensing.



Abdelhak M. Zoubir (S'87–M'92–SM'97–F'08) received the Dr.-Ing. degree from Ruhr-Universität Bochum, Bochum, Germany, in 1992.

He was with the Queensland University of Technology, Brisbane, Australia, from 1992 to 1998, where he was an Associate Professor. In 1999, he joined the Curtin University of Technology, Bentley, Australia as a Professor of telecommunications and was Interim Head of the School of Electrical and Computer Engineering, from 2001 until 2003. In 2003, he moved to Technische Universität

Darmstadt, Darmstadt, Germany, as Professor of signal processing and Head of the Signal Processing Group. His research interest lies in statistical methods for signal processing with emphasis on bootstrap techniques, robust detection and estimation and array processing applied to telecommunications, radar, sonar, car engine monitoring, and biomedicine.

Dr. Zoubir is a Fellow of the IEEE for contributions to statistical signal processing and an IEEE Distinguished Lecturer (Class 2010–2011). He authored or coauthored over 300 journal and conference papers on these areas, two of which, published in the IEEE TRANSACTIONS ON SIGNAL PROCESSING, received the Young Author Best Paper Award from the IEEE Signal Processing Society. He was Technical Chair of the 11th IEEE Workshop on Statistical Signal Processing (SSP 2001), General Co-Chair of the 3rd IEEE International Symposium on Signal Processing and Information Technology (ISSPIT 2003) and of the 5th IEEE Workshop on Sensor Array and Multichannel Signal Processing (SAM 2008). He is the Technical Co-Chair of ICASSP-14 to be held in Florence, Italy. He was an Associate Editor of the IEEE TRANSACTIONS ON SIGNAL PROCESSING (1999–2005), a member of the Senior Editorial Board of the IEEE JOURNAL ON SELECTED TOPICS IN SIGNAL PROCESSING (2009–2011), and he currently serves on the Editorial Boards of the European Association of Signal Processing (EURASIP) journals *Signal Processing* and the *Journal on Advances in Signal Processing*. He is the Editor-in-Chief of the IEEE SIGNAL PROCESSING MAGAZINE (2012–2014). He was the Chair of the IEEE SPS Technical Committee Signal Processing Theory and Methods (2010–2011), its Vice-Chair (2009–2010) and its member (2003–2008) and a member of the IEEE SPS Technical Committee Sensor Array and Multichannel Signal Processing (SAM) (2007–2012). He also serves on the Board of Directors of the EURASIP. He was the Guest Co-Editor of three special issues on topics in statistical signal processing, one of which is on the bootstrap that appeared in a special issue in the IEEE SIGNAL PROCESSING MAGAZINE in 2007.



Ahmed A. Mostafa (S'08) received the B.Sc. and M.Sc. degrees in electrical engineering from the Arab Academy for Science and Technology, Alexandria, Egypt, in 1997 and 2004, respectively. He is currently working toward the Ph.D. degree in the area of image processing and target detection at the Signal Processing Group of Technische Universität, Darmstadt, Germany.

He worked as an Instructor and Information Technology Training and Project Manager in the Arab Academy for Science and Technology.